npj | 2D Materials and Applications

www.nature.com/npj2dmaterials

ARTICLE OPEN

Origins of genuine Ohmic van der Waals contact between indium and MoS_2

Bum-Kyu Kim[1,7], Tae-Hyung Kim[2,7], Dong-Hwan Choi[1,3,7], Hanul Kim[3], Kenji Watanabe[4], Takashi Taniguchi[5], Heesuk Rho[3], Ju-Jin Kim[3]✉, Yong-Hoon Kim[2]✉ and Myung-Ho Bae[1,6]✉

The achievement of ultraclean Ohmic van der Waals (vdW) contacts at metal/transition-metal dichalcogenide (TMDC) interfaces would represent a critical step for the development of high-performance electronic and optoelectronic devices based on two-dimensional (2D) semiconductors. Herein, we report the fabrication of ultraclean vdW contacts between indium (In) and molybdenum disulfide (MoS_2) and the clarification of the atomistic origins of its Ohmic-like transport properties. Atomically clean In/MoS_2 vdW contacts are achieved by evaporating In with a relatively low thermal energy and subsequently cooling the substrate holder down to ~100 K by liquid nitrogen. We reveal that the high-quality In/MoS_2 vdW contacts are characterized by a small interfacial charge transfer and the Ohmic-like transport based on the field-emission mechanism over a wide temperature range from 2.4 to 300 K. Accordingly, the contact resistance reaches ~600 Ω µm and ~1000 Ω µm at cryogenic temperatures for the few-layer and monolayer MoS_2 cases, respectively. Density functional calculations show that the formation of large in-gap states due to the hybridization between In and MoS_2 conduction band edge states is the microscopic origins of the Ohmic charge injection. We suggest that seeking a mechanism to generate strong density of in-gap states while maintaining the pristine contact geometry with marginal interfacial charge transfer could be a general strategy to simultaneously avoid Fermi-level pinning and minimize contact resistance for 2D vdW materials.

npj 2D Materials and Applications (2021)5:9 ; https://doi.org/10.1038/s41699-020-00191-z

INTRODUCTION

Layered semiconducting transition-metal dichalcogenides (TMDCs) such as MoS_2, WSe_2, and $MoTe_2$ have been extensively studied for the future development of low-power and high-performance electronic and optoelectronic applications[1–3]. However, establishing a reliable Ohmic contact between metals and TMDCs remains a critical challenge[4,5]. For instance, in reducing the Schottky barrier height (ϕ_{SB}) for TMDCs, efforts to identify metals with appropriate work functions Φ_{metal} (e.g. $\Phi_{Sc} \approx 3.5$ eV for Sc and $\Phi_{Ti} \approx 4.3$ eV for Ti) based on the electron affinity of monolayer (1L) and few-layer TMDCs (e.g. monolayer MoS_2: $\chi_{1L\,MoS_2} \approx 4$ eV, multilayer MoS_2: $\chi_{ML\,MoS_2} \approx 4.3$ eV) have not been effective because of the strong Fermi-level pinning (FLP) effect[6,7]. While various approaches have been explored to overcome this problem, including molecular doping[8], tunnel-barrier insertion[9,10], fabrication of graphene contacts[11,12], and TMDC phase changes[13], recent studies have shown that the formation of an ideal or defect-free metal-TMDC van der Waals (vdW) contact through the transfer of atomically flat metal thin films significantly improves the contact properties[14–16]. In these advances, it was important to recognize that the conventional thermal evaporation process of metals typically introduces crystalline defects in TMDCs and leads to an uncontrollable ϕ_{SB} (or FLP) and high contact resistance[7,14]. Meanwhile, several groups overcame the challenge and showed that the thermal-evaporation process of indium (In) can lead to clean vdW-type contacts for TMDCs with very low contact resistance values[17–19]. However, regarding our initial report on the achievement of Ohmic-like three-dimensional (3D) In-2D MoS_2 contact[18], question was raised in that the origins of the low contact resistance through the In–MoS_2 vdW contact are unclear.

Here, we prepare an ultraclean vdW contact between In and MoS_2 using an improved evaporation method, and clarify through extensive transport measurements and computations the nature and origins of Ohmic transport characteristics from In/MoS_2 vdW contacts. We prepare the high-quality vdW In/MoS_2 interface by lowering the temperature (T) of the substrate holder to ~100 K during the metal deposition process and utilizing the relatively low In evaporation T of ~530 °C. The In/MoS_2 interface is then characterized by the transmission electron microscope (TEM) and Raman measurements as well as density functional theory (DFT) calculations. DFT calculations show that in comparison with the Au/MoS_2 counterpart, the In/MoS_2 contact induces an order of magnitude smaller charge transfer, which is consistent with the Raman spectroscopy data. For both mono- and few-layer MoS_2 devices prepared through our approach, we find that the contact resistance decreases with decreasing T from room temperature to $T = 100$ K and 2.4 K, reaching to 1 kΩ µm and 0.6 kΩ µm, respectively. This behavior indicates the Ohmic-like character at the In/MoS_2 contact and the field emission is the dominant charge transport mechanism at the In/MoS_2 contact. We finally identify from DFT calculations large in-gap states originating from the hybridization between MoS_2 conduction-band-edge and In Fermi-level states, which provides a mechanism to achieve an Ohmic contact in spite of the marginal interfacial charge transfer.

[1]Korea Research Institute of Standards and Science, Daejeon 34113, Republic of Korea. [2]School of Electrical Engineering, Korea Advanced Institute of Science and Technology, 291 Daehak-ro, Yuseong-gu, Daejeon 34141, Republic of Korea. [3]Department of Physics, Research Institute of Physics and Chemistry, Jeonbuk National University, Jeonju 54896, Republic of Korea. [4]Research Center for Functional Materials, National Institute for Materials Science, 1-1 Namiki, Tsukuba 305-0044, Japan. [5]International Center for Materials Nanoarchitectonics, National Institute for Materials Science, 1-1 Namiki, Tsukuba 305-0044, Japan. [6]Department of Nano Science, University of Science and Technology, Daejeon 34113, Republic of Korea. [7]These authors contributed equally: Bum-Kyu Kim, Tae-Hyung Kim, Dong-Hwan Choi. ✉email: jujinkim@chonbuk.ac.kr,; y.h.kim@kaist.ac.kr; mhbae@kriss.re.kr

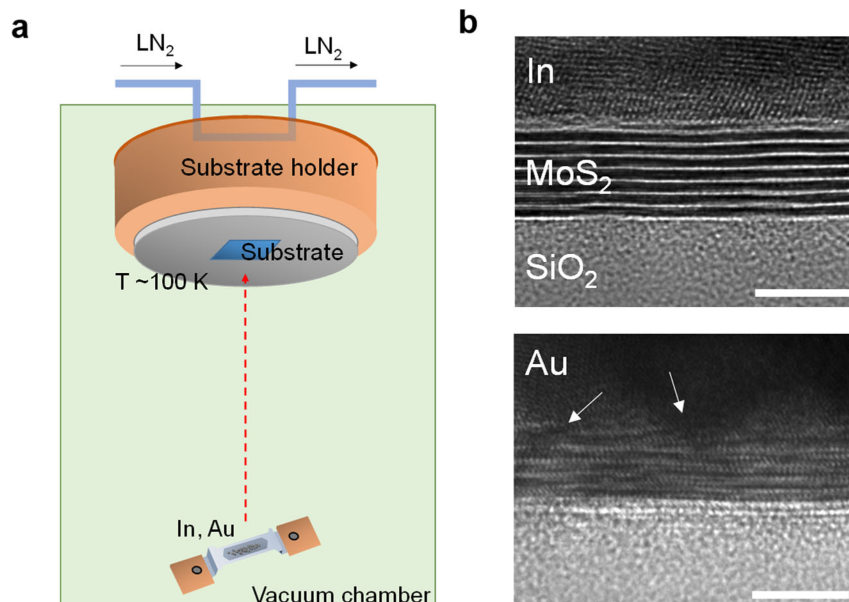

Fig. 1 Metal deposition on MoS_2. **a** In (Au) evaporation in a vacuum chamber with a liquid-nitrogen cooled sample holder. **b** Top and bottom: cross-sectional TEM images of the In/MoS_2 and Au/MoS_2 interfaces, respectively. Scale bar: 5 nm.

RESULTS AND DISCUSSION

Characterizations of the ultraclean In/MoS_2 interface

We fabricated MoS_2 field-effect transistors (FETs) on hexagonal boron nitride (*h*-BN) flakes, where the *h*-BN flakes were deposited onto a 300-nm-thick SiO_2/Si substrate by mechanical exfoliation. We then transferred a few-layer MoS_2 flake (HQ-graphene, Inc.) onto a selected *h*-BN flake[12,20]. For the electrical measurements, we deposited 100-nm-thick In electrodes across the MoS_2 channel, where the substrate holder was kept at ~100 K by flowing liquid nitrogen through it (see Fig. 1a). The substrate cooling process leads to an important result, namely a highly uniform surface morphology of In film. This contrasts strongly with the usage of a room-temperature holder that produces a segregated granular film for at least up to ~70 nm thickness, as reported in our previous work (also see Supplementary Fig. 1)[21]. The upper panel of Fig. 1b shows a cross-sectional TEM image of the In/few-layered MoS_2 junction, which clearly shows an atomically separated interface between In and MoS_2 layers without any metal invasion into the MoS_2 layers. Whereas crystal-lattice disorders that cause defect-induced gap states and FLP typically occur during the high-temperature deposition process of evaporated metal atoms with high thermal energy[7,14], the In deposited at a relatively low thermal energy could apparently provide a clean vdW interface without disorder or defect. For instance, whereas the evaporation temperature of Au at 10^{-7} Torr is ~860 °C, only ~530 °C is required for the evaporation of In at the same pressure. For comparison, we prepared an Au/few-layered MoS_2 junction, where the substrate holder was also kept at ~100 K during Au deposition. The lower panel of Fig. 1b shows a TEM image of the Au/MoS_2 junction, where we observe that the invasion of Au atoms during the deposition process produces atomic defects at the first and second layers from the MoS_2 interface, like previous studies[14].

To further characterize the quality of In/MoS_2 interface, we applied the Raman spectroscopy for both the pristine and In-covered MoS_2 regions to estimate doping effect at the metal contacts. It is known that the A_{1g} phonon peak of MoS_2 exhibits a red shift and its width broadens with electron doping[22,23]. Figure 2a, b shows the optical images of, respectively, 1L- and bilayer (2L)-MoS_2 (indicated by regions bounded with dashed black lines) prepared on SiO_2 and partially covered with 5-nm-thick In (indicated by regions bounded with dashed white lines). Figure 2c, d shows the A_{1g} energy maps for the 1L- and 2L-MoS_2, respectively. The In-covered region shows a relatively lower energy than the non-covered region, i.e., $\Delta\omega \approx -0.3$ and $-1\ cm^{-1}$ for the 1L- and 2L-MoS_2, respectively (see Supplementary Fig. 2 for representative Raman spectra for a 1L-MoS_2). In the upper panel of Supplementary Fig. 2a, we also show the E^1_{2g} energy map of the 1L-MoS_2, which indicates relatively negligible difference between the In-covered and non-covered regions. For the biaxial strain, the red shift of the E^1_{2g} Raman mode corresponding to the in-plane vibration is more sensitive than the A_{1g} mode (out-of-plane vibration)[24,25]. For the in- and out-of-plane compressive strains, both modes should show blue shifts[26]. In our case, however, we observed a relatively strong red shift of the A_{1g} mode than that of the E^1_{2g} mode, which has been interpreted as a doping effect[22]. For instance, Chakraborty et al.[22] reported that the A_{1g} mode softens with doping at a rate of ~0.2 cm^{-1} per $10^{12}\ cm^{-2}$ for 1L-MoS_2, whereas the E^1_{2g} mode is relatively insensitive to the doping. We thus conclude that the 1L-MoS_2 region covered by In was doped by electrons at a density of $\sim+1.5\times10^{12}$ electrons cm^{-2} (electron accumulation in MoS_2). The full-width at half-maximums, Γ, in Fig. 2e, f also show consistent results. For instance, the In-covered region shows a relatively broader Γ than the non-covered region for both 1L- and 2L-MoS_2, implying electron doping. This In-to-MoS_2 electron transfer feature will be further discussed below based on DFT calculations and shown to be another strong indication of ultraclean vdW contacts.

Charge redistribution at the In/MoS_2 interface

To extract the atomistic information of the In/MoS_2 vdW contact and contrast them with those of the Au/MoS_2 counterpart, we carried out DFT calculations for the vertical In/MoS_2 and Au/MoS_2 interface models and applied several analysis methods[27,28]. In Fig. 3a, b top panels, we show the fully optimized In/MoS_2 and Au/MoS_2 contact models, respectively (see details in Supplementary Figs. 3, 4 and Table 1). First, compared to the Au/MoS_2 case, we find in the optimized In/MoS_2 atomic structure negligible structural distortions at the rightmost metal atomic layer (see also Supplementary Fig. 3). As supported by the DFT-estimated binding energy[29,30] as well as the explicit experimental demonstration for the transferred Au electrode[14], Au is a representative metal that forms vdW-type interactions

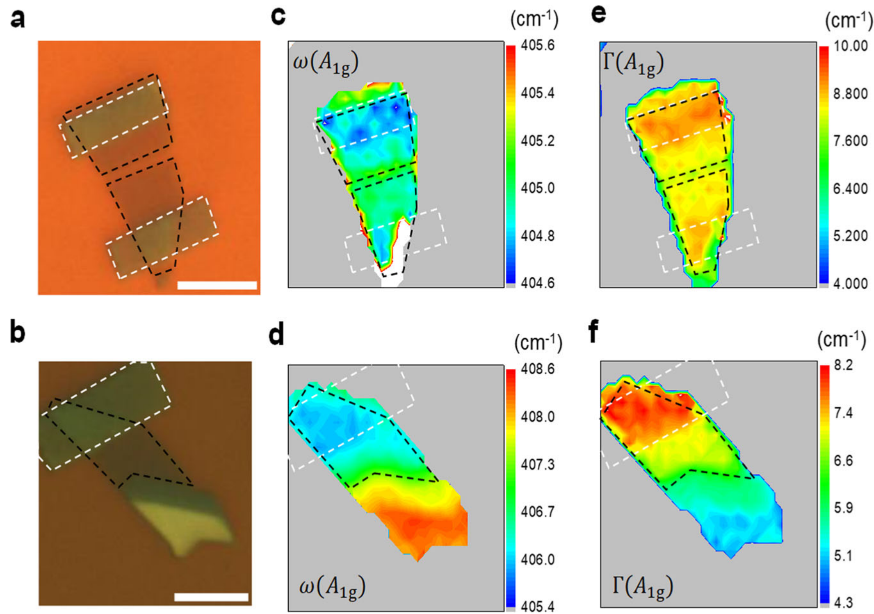

Fig. 2 Raman spectroscopy for In/MoS_2. **a**, **b** Optical images of 1L- and 2L-MoS_2 (dashed black-boxed region) on SiO_2 substrates, respectively. White boxed regions: 5-nm-thick In-deposited regions. Scale bar: 5 µm. **c**, **d** A_{1g} energy (ω) maps for 1L- and 2L-MoS_2, respectively. **e**, **f** Full-width at half-maximum (Γ) maps of A_{1g} for 1L- and 2L-MoS_2, respectively.

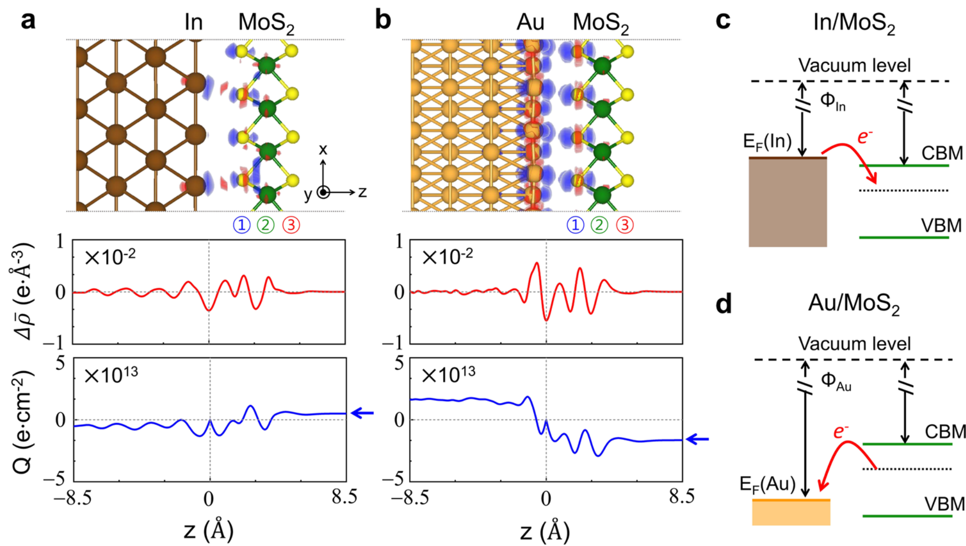

Fig. 3 Charge redistribution properties of the In/MoS_2 interface from DFT calculations. For the **a** In/MoS_2 and **b** Au/MoS_2 interface models, (top panels) DFT-optimized atomic geometries, (middle panels) plane-averaged charge density differences $\Delta\bar{\rho}$, and (bottom panels) total charge transfers Q (bottom) are shown. In the top panels, interfacial charge transfers are overlaid over the atomic structures, with the electron accumulation and depletion regions represented by the red and blue colors, respectively. The isosurface level is $1 \times 10^{-3}\, e\,\text{Å}^{-3}$. Schematics of the metal and MoS_2 band levels before contact for the **c** In/MoS_2 and **d** Au/MoS_2 cases. Dotted lines represent the MoS_2 charge neutrality levels, whose energetic positions with respect to the In and Au Fermi levels E_F result in the In-to-MoS_2 and MoS_2-to-Au interfacial charge transfers.

with MoS_2. Accordingly, the comparatively smaller In contact-induced structural perturbations consistently seen in our experiment and simulation indicate that In forms even more ideal vdW interactions with MoS_2 than Au.

To quantify this conclusion, we calculated the real-space charge density differences ($\Delta\rho$) at the metal/MoS_2 interfaces according to

$$\Delta\rho = \rho_{\text{metal}/MoS_2} - \left(\rho_{MoS_2} + \rho_{\text{metal}}\right) \quad (1)$$

and overlaid the results on the atomic structures in Fig. 3a, b top panels. The plane-averaged $\Delta\bar{\rho}(z)$ for the In/MoS_2 and Au/MoS_2 contact cases are also presented in Fig. 3a, b middle panels, respectively. A positive (negative) $\Delta\bar{\rho}$ indicates a gain (loss) in electron density, and we find stronger charge redistributions in the Au/MoS_2 contact compared with the In/MoS_2 counterpart. Examining the distribution of $\Delta\bar{\rho}$ between the surface metal layers and the interfacial S layer ① of MoS_2, we further note that due to the "push-back" effect arising from Pauli repulsion there appear charge-depleted (negative $\Delta\bar{\rho}$) 2D plane regions close to the metal surfaces (denoted by vertical dotted lines)[28,30].

Using the minimum-$\Delta\bar{\rho}$ layers as the reference planes ($z = 0$), we calculated along the MoS_2 direction the position-dependent

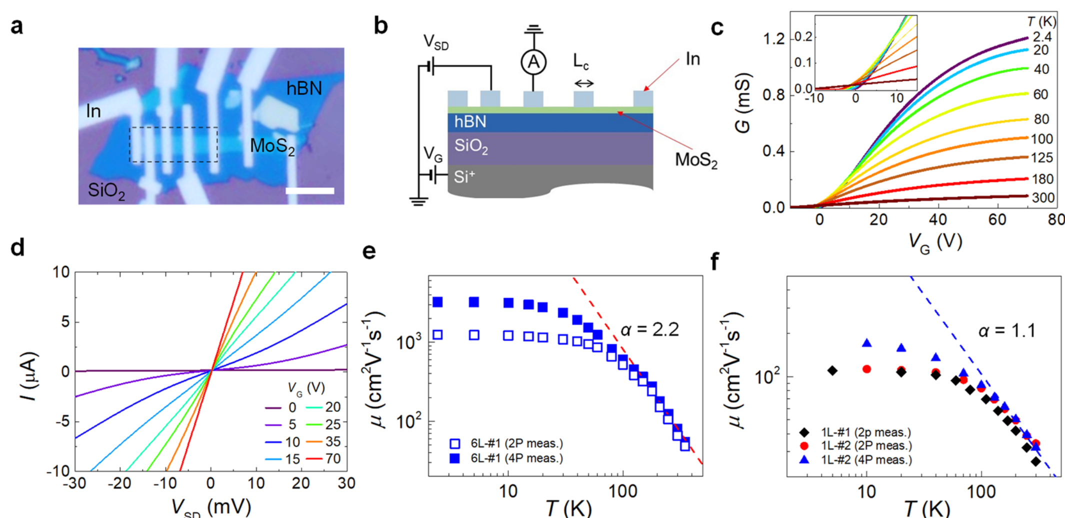

Fig. 4 Basic electrical properties of a few-layer MoS_2 field-effect transistor. **a** Optical image of a 6L-#1 MoS_2 device with multiple In contacts. Scale bar: 5 μm. **b** Schematic of 6L-#1 MoS_2 device for the transfer length method (TLM). Here, L_c (=1 μm) is the length of contact electrode. The measurement scheme shows the two-probe measurement for the $L_2 = 1$ μm channel. **c** Conductance (G) as a function of the back-gate voltage (V_G) at various temperatures. Inset: G–V_G curves near the metal–insulator crossover region. **d** I–V_{SD} curves for various V_G at $T = 2.4$ K. **e**, **f** Mobility (μ) as a function of temperature (T) in log scale for 6L and 1L devices, respectively. The red and blue dashed lines in **e** and **f** are fitting lines with the relation of $\mu(T) \propto T^{-\alpha}$ with $\alpha = 2.2$ and 1.1 for 6L and 1L devices, respectively.

accumulated interfacial charge transfers according to

$$Q(z) = \int_0^z \Delta\bar{\rho}(z')dz', \quad (2)$$

and displayed the results in Fig. 3a, b bottom panels. Note that a positive (negative) Q indicates a metal-to-MoS_2 (MoS_2-to-metal) electron transfer upon establishing the metal/MoS_2 interface[27]. We then find that In induces a marginal electron transfer of $+5.0 \times 10^{12}$ electrons cm^{-2} to MoS_2 (left blue arrow in Fig. 3a bottom panel), which is in good quantitative agreement with the above-described estimate of $\sim 1.5 \times 10^{12}$ electrons cm^{-2} from Raman measurement (see Fig. 2). The marginal electron transfer leads to a weakened FLP, compared to an Au case. For the Au/MoS_2 case, the direction of charge transfer is reversed (electron depletion in MoS_2), and its magnitude is significantly enhanced to -1.7×10^{13} electrons cm^{-2} (left blue arrow in Fig. 3b bottom panel). These opposite MoS_2 doping characters of In and Au can be understood in terms of the alignment of the MoS_2 charge neutrality level $\phi^*_{1L\,MoS_2} \approx 4.78$ eV with respect to the metal work functions $\Phi_{In} \approx 4.1$ eV and $\Phi_{Au} \approx 5.1$ eV[31], as schematically shown in Fig. 3c, d, respectively (see Supplementary Figs. 5, 6, and 7).

Electrical properties of a MoS_2 FET

Figure 4a and b shows a photograph of a MoS_2 FET on a 22-nm-thick h-BN flake and schematic for the electrical measurement configuration, respectively. The number of MoS_2 layers was estimated to be six (6L-#1 MoS_2; see Supplementary Fig. 8). The multiple electrodes for the six-layer (6L) MoS_2 flake with different intervals between two neighboring electrodes were designed to measure the contact resistance via the transfer-length method (TLM)[13], i.e., four FETs with different channel lengths ($L_1 = 0.5$ μm, $L_2 = 1$ μm, $L_3 = 1.5$ μm, and $L_4 = 2$ μm from the left channel in the region indicated by a dashed box) with a fixed metal contact length (L_c) as 1 μm. Here, the widths (W) of all channels were nearly identical at 2 μm. Figure 4c shows the two-probe conductance as a function of the back-gate voltage (G–V_G) of the L_2-FET with a source–drain voltage (V_{SD}) of 30 mV at various temperatures. The conductance decreased for negatively increasing V_G and reached zero near $V_G \approx 0$ V throughout the investigated temperature range, which indicates that the electrical carriers are electrons. The two-probe conductance increased with decreasing T at a given V_G for $V_G > 10$ V, i.e., the device exhibited a metallic behavior. However, the opposite behavior was observed near a depletion region of $0 < V_G < 10$ V (see the inset of Fig. 4c), representing an insulating character. These behaviors are consistent with the current–voltage (I–V_{SD}) curves for various V_G values at $T = 2.5$ K in Fig. 4d. For instance, the I–V_{SD} curves for $V_G > 10$ V and $0 < V_G < 10$ V show linear and nonlinear characteristics, respectively. We consider that the linearity and non-linearity originate from the field and thermionic emission through a Schottky barrier, respectively. The four-probe measurements for the L_2 channel also showed a similar V_G value for the metal–insulator crossover location (see Supplementary Fig. 9). This result indicates that the transport in the MoS_2 channel near the conduction-band edge also contributes to the crossover behavior, as well as the Schottky barrier. We also extracted the on/off ratio of $\sim 10^5$ and 10^3–10^5 of other monolayer (1L-#1) and 6L (6L-#2) devices, respectively, as shown in Supplementary section 5. The ratios satisfy a condition for logic gate applications. On the other hand, the on-current densities of 1L-#1 MoS_2 and 6L-#2 MoS_2 devices reached ~60 μA $μm^{-1}$ and ~200 μA $μm^{-1}$, respectively. The 6L-#2 MoS_2 device also showed a stability against aging at least for 40 days for -1 V $< V_{SD} < 1$ V (see Supplementary Fig. 11d).

In Fig. 4e, we show the field-effect mobility (μ) of the 6L-#1 MoS_2 device as a function of T obtained from the two-probe (open squares) and four-probe (closed squares) measurement schemes. The mobility was obtained at the local maximum location in the μ–V_G curves (see Supplementary Fig. 12). For $T > 100$ K, in both cases, the data were fitted with a relation of $\mu(T) = \mu_0 T^{-\alpha}$ with $\alpha = 2.2$ as shown by the dashed red line. This value is close to the expected value for bulk MoS_2 ($\alpha = 2.6$) with the optical phonon scattering as a dominant scattering mechanism[12,32,33]. At room T, $\mu \sim 50\ cm^2\,V^{-1}\,s^{-1}$ values were obtained for both cases. However, the two-probe and four-probe μ values were saturated with decreasing temperature in the region $T < 20$ K at 1200 and 3200 $cm^2\,V^{-1}\,s^{-1}$, respectively. The saturation behavior in low-T regions is known to occur when the impurity scattering assumes a dominant role while the phonon-scattering effect is suppressed[34]. By contrast, the mobility for two different 1L MoS_2 devices (1L-#1 and 1L-#2; see Supplementary Figs. 10c, 13, respectively) displayed in Fig. 4f show a T dependence with $\alpha = 1.1$ for $T > 100$ K, which is

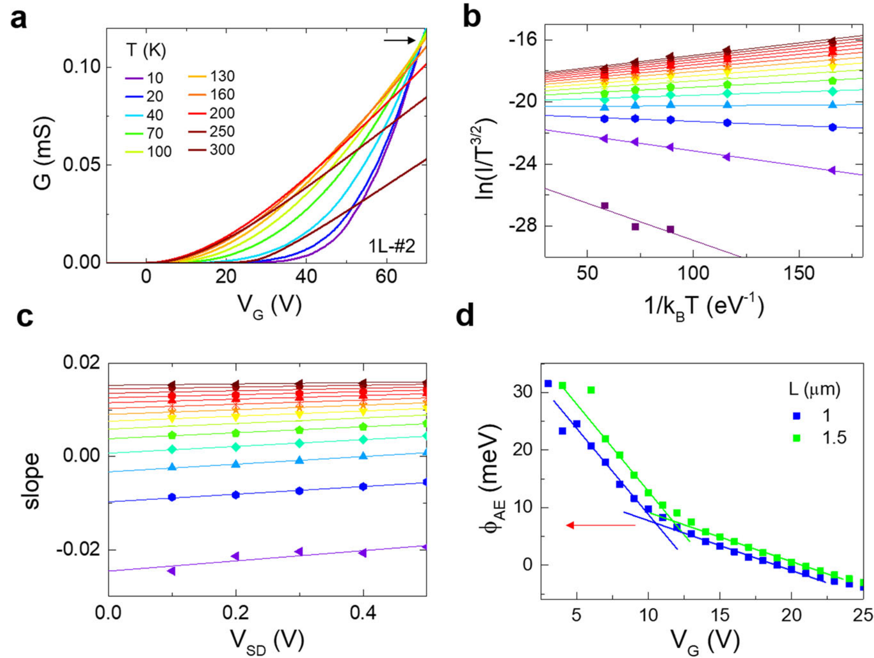

Fig. 5 Schottky barrier height at In/MoS_2 contacts. a G–V_G curves at various temperatures obtained from the $L = 1$ μm channel of 1L-#2 MoS_2 device, indicated by a dashed box in Supplementary Fig. 13a. **b** Scattered points: $\ln(I/T^{3/2})$ as a function of $1/k_BT$ with $V_{SD} = 0.5$ V from $V_G = 0$ V to 70 V with 5 V spacing (from bottom to top) obtained from the $L = 1$ μm channel. Solid lines: fitting result to obtain slope values for each V_G value. **c** Scattered points: slope as a function of V_{SD} for various V_G (5 V to 70 V with 5 V spacing from bottom to top). Solid lines: fitting result to obtain ϕ_{AE} at $V_{SD} = 0$ V for each V_G value. **d** ϕ_{AE} as a function of V_G for $L = 1$ and 1.5 μm channels. The arrow indicates the ϕ_{SB} (~7 meV) for the 1L-#2 MoS_2 device.

close to the prediction of the acoustic phonon scattering becoming a dominant scattering mechanism for a monolayer MoS_2 (ref. [33]).

For comparison, we also fabricated MoS_2 devices with In contacts covered with Au, where the sample holder was a copper block prepared without a liquid-nitrogen cooling process. In this case, we found that the reproducibility was not high enough to obtain the consistent Ohmic-like behavior in the I–V_{SD} curves, confirming the critical role of our substrate cooling technique (see Supplementary Fig. 14).

Schottky barrier height at In/MoS_2 contacts

We evaluated ϕ_{SB} at the In/MoS_2 interface because this parameter plays a critical role in determining the contact resistance between a metal and a semiconductor[4]. For this purpose, it is necessary to measure the activation energy (ϕ_{AE}) at the contacts in the thermionic emission region[6]. Here, because the V_G range for the insulating region is larger than that of the 6L-#1 MoS_2 device (see Fig. 4c), we used the 1L-#2 MoS_2 device with the $L = 1$ μm channel shown in Supplementary Fig. 13a. Figure 5a shows the resulting G–V_G curves for various temperatures obtained by the two-probe measurement. In this case, the crossover V_G between the insulating and metallic regions was located at a relatively higher V_G (~65 V) than that of the 6L-#1 MoS_2 device, as indicated by an arrow. The G values increased with increasing T for $T < 130$ K at $V_G < 65$ V and decreased for $T > 200$ K in the examined V_G range. When the thermionic emission is dominant, the current crossing a metal/2D system is described by the relation

$$I_d = A^* T^{3/2} \exp\left(\frac{-e\phi_{AE}}{k_B T}\right)\left[\exp\left(\frac{eV_{SD}}{\eta k_B T}\right) - 1\right], \quad (3)$$

where A^* is the Richardson constant, e is the elementary charge, k_B is the Boltzmann constant, and η is the ideality factor that accounts for a lower barrier height due to image charging[12]. Figure 5b shows $\ln(I/T^{3/2})$ as a function of $1/k_BT$ at $V_{SD} = 0.5$ V for various V_G values from 0 V to 70 V with 5 V spacing (from bottom to top). The slopes of $\ln(I/T^{3/2}) - 1/k_BT$ curves are related to ϕ_{AE} as $\phi_{AE} = V_{SD}/\eta$ − slope. After obtaining the slopes corresponding to representative V_{SD} values, we plotted the slope as a function of V_{SD} for various V_G (5 V to 70 V with 5 V spacing from bottom to top) to obtain ϕ_{AE} at $V_{SD} = 0$ V, as shown in Fig. 5c. Finally, we plotted ϕ_{AE} vs. V_G to obtain ϕ_{SB}, as blue squares in Fig. 5d. Near the depletion region, ϕ_{AE} is linearly lowered with increasing V_G when the thermally activated transport is dominant and changes its slope when the field-emission transport is accounted at the Schottky barrier. Thus, the crossover point between them occurs when the band flattens, where, the value of ϕ_{AE} becomes equal to the value of ϕ_{SB}[6]. To find V_G making the band flat, we plotted two linear blue lines on the blue squares in Fig. 5d. The two curves meet at $V_G \approx 10$ V, where the flat band is believed to form, and we estimated $\phi_{SB} \approx 7$ meV at the corresponding ϕ_{AE} for the In/MoS_2 ($n = 1$) contact. In addition, we also obtained a similar value for the $L = 1.5$ μm channel as indicated by green squares and green fit lines in Fig. 5d (see also Supplementary Fig. 13a). This value is in a similar range obtained from a Co/h-BN contact with a monolayer MoS_2 (ref. [10]). Such a low ϕ_{SB} at the In/MoS_2 contact could allow the field-emission to play a dominant role for the transport across the In/MoS_2 contact.

Contact resistance at In/MoS_2 contacts

On the basis of the TLM measurements (see Supplementary Fig. 15) with multiple channels (see Fig. 4a), we extracted the contact resistance (R_cW) as a function of n_e of the 6L-#1 MoS_2 device at representative temperatures; the results are shown in Fig. 6a (solid squares; see also Supplementary Table 2). Here, n_e was estimated from the relation $n_e = (e\mu R_{sh})^{-1}$. We note that, for the consistency, the sheet resistance R_{sh} as well as mobility μ were obtained from the four-probe data, although R_{sh} could have been extracted from the TLM method. The obtained contact resistance includes serial resistances of In and Ti/Au electrodes (see supplementary Fig. 16). At a given T, R_cW decreased with increasing n_e. The contact

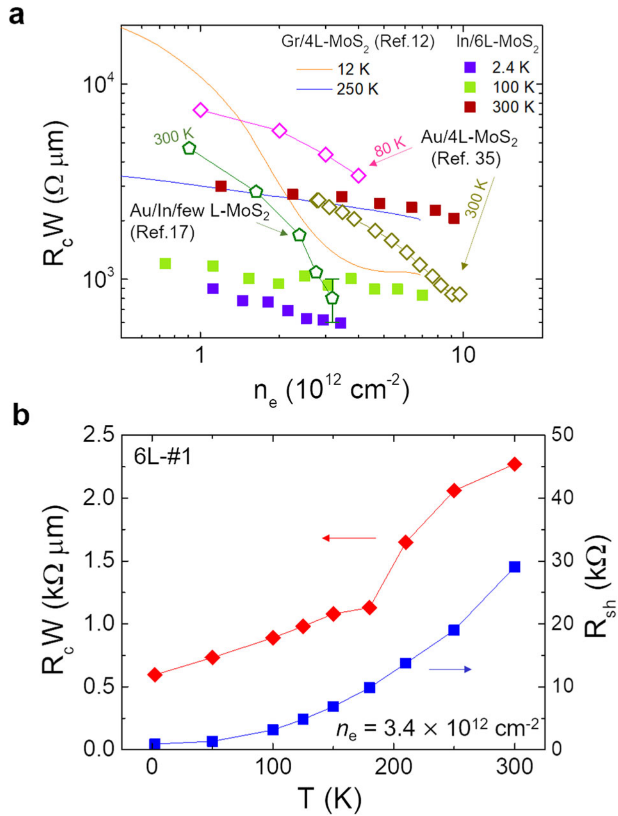

Fig. 6 Contact resistance with carrier density at In/MoS$_2$ contacts. **a** Contact resistance (R_cW) as a function of carrier density (n_e) of 6L-#1 MoS$_2$ device at various temperatures (scattered solid squares) with other works (solid curves: graphene(Gr)/4L-MoS$_2$, opened diamonds: Au/4L-MoS$_2$, opened pentagons: Au/In/few L-MoS$_2$). **b** R_cW and sheet resistance (R_{sh}) of 6L-#1 MoS$_2$ device as a function of T at $n_e = 3.4 \times 10^{12}$ cm^{-2}.

resistance is given by[4,5]

$$R_cW(n_e, T) = \sqrt{R_{sh}(n_e, T)\rho_c(n_e, T)}, \quad (4)$$

which is only valid for $L_c \gg L_T$. Here, ρ_c is the specific contact resistivity and L_T ($=\sqrt{\rho_c/R_{sh}}$) is the transfer length, which represents the average distance that charge carriers flow in a semiconductor beneath the contact before they completely transport to the electrode. Supplementary Fig. 15c shows that our device satisfied this condition with $L_c \approx 1$ μm and $L_T \approx 0.1$ μm. Equation (4) implies that R_cW decreases with increasing n_e because both R_{sh} and ρ_c generally decrease with increasing n_e. At a fixed n_e, the thermionic emission charge transport mechanism across the Schottky barrier predicts that R_cW will increase with decreasing T because the thermionic emission will be suppressed with lowering T[35]. On the other hand, R_cW in our measurements decreased with decreasing T, as shown by scattered red diamonds in Fig. 6b for the case measured at $n_e = 3.4 \times 10^{12}$ cm^{-2}. The contact resistance decreased from 2.3 to 0.6 kΩ μm when T was decreased from room temperature to 2.4 K. This behavior, which has been reported in several previous works such as graphene/MoS$_2$ (ref. [12]) and Pd/graphene contacts[36], is considered as an evidence for the non-dominant role of thermionic emission for the transport across a contact. Scattered squares in Fig. 6b also show R_{sh} as a function of T at $n_e = 3.4 \times 10^{12}$ cm^{-2}, where R_{sh} decreased with decreasing T because the phonon scattering is reduced.

Sheet resistance vs. specific contact resistivity

We further analyzed the mechanism of charge transport across In/MoS$_2$ contacts with experimental data in detail. We first examined which component between R_{sh} and ρ_c predominantly determines the contact resistance of the In/MoS$_2$ contact. For comparison, we included in Fig. 6a other values reported in the literature; graphene(Gr)/four-layer (4L)-MoS$_2$ contact[12], Au/4L-MoS$_2$ (ref. [35]) and Au/In/few-layer MoS$_2$ (ref. [17]). In the case of Gr/4L-MoS$_2$, the graphene functions as a work-function-controllable contact material, which leads to a lower contact resistance, i.e., $R_cW \approx 1$ kΩ μm at $n_e > 4 \times 10^{12}$ cm^{-2} and $T = 12$ K (see the red curve in Fig. 6a). Although both the Gr-and In-contact MoS$_2$ devices gave a similar minimum R_cW at cryogenic temperatures, we conclude that the transport mechanisms at the contacts rather differ from each other. For the In/MoS$_2$ contact case, R_cW decreased with decreasing T in the examined n_e range, representing the field emission (or tunneling) for all examined T and n_e ranges. However, the $R_cW - n_e$ curves obtained at $T = 12$ and 250 K for the Gr/4L-MoS$_2$ device suggest that the left and right sides with respect to $n_e \approx 2 \times 10^{12}$ cm^{-2} followed the thermionic and field emissions at the contact, respectively. At $T = 12$ K for the Gr/4L-MoS$_2$ device, although the R_cW of ~1 kΩ μm was relatively insensitive to the variation of n_e in the range from 4×10^{12} to 7×10^{12} cm^{-2}, it rapidly changed from 1 kΩ μm to 6 kΩ μm when n_e decreased from 3×10^{12} cm^{-2} to 1.5×10^{12} cm^{-2}. In the case of the Au/4L-MoS$_2$ contact, on the other hand, R_cW was increased with decreasing T representing the thermionic emission for $n_e < 4 \times 10^{12}$ cm^{-2}. While the Au/In/few layer-MoS$_2$ contact provides a relatively low-R_cW level for $n_e > 1.5 \times 10^{12}$ cm^{-2} at $T = 300$ K, it is hard to judge the transport mechanism for the In contact because of the absence of the T-dependence of R_cW in the experiment. Then, for the In/6L-#1 MoS$_2$ device, the R_cW was lowered with decreasing T at a given n_e for 1×10^{12} cm$^{-2} < n_e < 1 \times 10^{13}$ cm^{-2}, representing an Ohmic-like behavior based on the field-emission mechanism in the examined n_e region. In our In/6L-MoS$_2$ device (see Fig. 7a), R_{sh} varies in the range from 1 to 80 kΩ when ρ_c only varies from 5×10^{-6} to 5×10^{-7} Ω cm^2, as shown by two dashed lines, for R_cW changing from 0.6 to ~3 kΩ μm. This result indicates that R_{sh} plays a dominant role in determining R_cW in the field-emission region.

We also obtained R_cW from the 1L-#2 MoS$_2$ device on a 40-nm-thick h-BN flake (see Fig. 7b and Supplementary Fig. 13 for the thickness profile). In Fig. 7b, the R_cW values were extracted via the TLM with three channels ($L = 0.5$, 1, 1.5 μm) as shown in Supplementary Fig. 13a. For three $V_{G\text{-th}}$ conditions of 35, 40, and 45 V, R_cW decreased with decreasing T in the range 250 ≥ T ≥ 100 K, representing the field emission. Here, $V_{G-th} = V_G - V_{th}$ and V_{th} is a threshold voltage. At $V_{G-th} = 45$ V, R_cW reached ~1 kΩ μm at $T = 100$ K as the minimum value obtained from the 1L-MoS$_2$ device. Although this value is similar to that obtained from the 6L-MoS$_2$ device at a similar T range (see Fig. 6a), the contact resistance for the monolayer MoS$_2$ is higher than that of multilayer MoS$_2$. The reason could be related to the relatively low affinity energy in the monolayer MoS$_2$. Interestingly, R_cW increased with decreasing T for $T < 100$ K under all V_{G-th} conditions. In this region, the MoS$_2$ channel also exhibited an insulating behavior in G–V_G curves for various temperatures of Fig. 5a for $V_G < 60$ V and $T < 100$ K. Thus, it indicates that the increase of R_{sh} with decreasing T in the insulating phase plays a dominant role in determining the contact resistance at $T < 100$ K. We note that this non-Ohmic behavior could not be improved by the contact engineering because the behavior originates from the intrinsic property of MoS$_2$ itself. This implies that the manipulation of the metal-insulator crossover gate voltage could be crucial to get a better contact property in a mono-layer MoS$_2$ device. In Fig. 7a (see also Supplementary Table 2), we compared the lowest achievable contact resistance as a function of R_{sh} from previous reports with

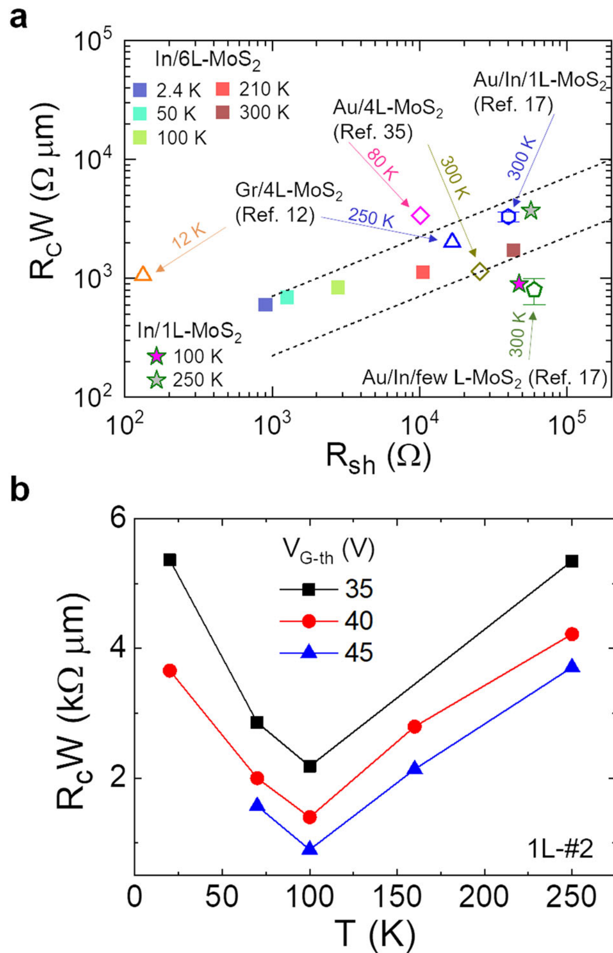

Fig. 7 Contact resistance with sheet resistance at In/MoS_2 contacts. a Minimum R_cW as a function R_{sh} of 6L-#1 and 1L-#2 MoS_2 devices at various temperatures (scattered solid squares and stars, respectively) with previous works (opened triangles: graphene (Gr)/4L-MoS_2, opened diamonds: Au/4L-MoS_2, opened pentagons: Au/In/few (1) L-MoS_2). The upper and lower dashed lines were obtained with $\rho_c = 5\times10^{-6}\,\Omega\,cm^2$ and $5\times10^{-7}\,\Omega\,cm^2$, respectively. **b** R_cW–T curves for various $V_{G\text{-}th}$ conditions of 1L-#2 MoS_2 device.

ours. For the In/MoS_2 device, the contact resistance decreased with decreasing R_{sh} and reached ~0.6 kΩ µm as the lowest value at R_{sh} ~ 1 kΩ and $T = 2.4$ K. At $T = 300$ K, on the other hand, the Au/In/few layer-MoS_2 device showed the lowest value of ~0.6 kΩ µm at R_{sh} ~ 60 kΩ. In addition, for monolayer cases, our In/1L-#2 MoS_2 contact provided 0.9–4 kΩ µm at R_{sh} ~ 50 kΩ, which are comparable to those obtained from the Au/In/1L-MoS_2 contact that showed ~3 kΩ µm at R_{sh} ~ 40 kΩ.

Atomistic origins of the field emission-dominated charge transport across In/MoS_2 contacts

Analyzing the electronic structures of the In/MoS_2 and Au/MoS_2 interfaces obtained from DFT calculations, we finally identify the atomistic mechanisms of the experimentally observed Ohmic-like charge transport behavior. It should be noted that, while there exist in the literature several theoretical studies that examined the Schottky barriers in metal/TMDC interfaces[30,37–40], the In/TMDC case has been rarely treated[41]. We show the calculated band structures at the In/MoS_2 and Au/MoS_2 contacts in Fig. 8a, b, respectively, and particularly display the projected bands of Mo-*4d* (green circles in Fig. 8a, b), In-*5p*$_z$ (wine filled circles in Fig. 8a), and Au-*6s* (orange circles in Fig. 8b) orbitals. From the band structures, one could determine the electron ϕ_{SB} by measuring the energy level difference between the conduction band minimum (CBM) edge (upper solid purple line) and the Fermi level E_F (dashed purple line) of metal/MoS_2 contacts. However, the comparison of the two bands indicate that identifying the electron ϕ_{SB} in the In/MoS_2 contact is a non-trivial matter due to the strong density of in-gap states appearing below and around the MoS_2 CBM region (green circles between CBM and E_F in Fig. 8a; note the absence of such in-gap states in the Au/MoS2 contact in Fig. 8b). To circumvent this difficulty, we first extracted the hole ϕ_{SB} from the In/MoS_2 junction band structure (see also Supplementary Fig. 5). Next, calculating the band structure of the pristine monolayer MoS_2 using the simulation cell of the corresponding In/MoS_2 junction model (Supplementary Fig. 6), we determined the electron ϕ_{SB} by subtracting the hole ϕ_{SB} from the calculated band gap of monolayer MoS_2 (1.94 eV) (Supplementary Fig. 7). The obtained electron ϕ_{SB} values were 0.31 eV and 0.72 eV for the In/MoS_2 and Au/MoS_2 junctions, respectively. The In/MoS_2 electron, ϕ_{SB} value of 0.31 eV is comparable to a previous estimate of 0.47 eV[41] and much larger than the experimentally identified marginal ϕ_{SB} values. We thus conclude that the experimentally observed ϕ_{SB} is an effective ϕ_{SB} that has been significantly reduced from the intrinsic ϕ_{SB} by strong density of in-gap states.

Having been identified as the distinguishing feature, the large in-gap states arising in the In/MoS_2 contact should be the source of the marginal effective ϕ_{SB} and Ohmic-like transport and deserve further attention. Disregarding this factor, for example, can lead to the conclusion that Au would form a better contact than In for MoS_2[41], but the in-gap states of the In/MoS_2 contact remains unexplored[37,38]. To examine the nature of in-gap states in the In/MoS_2 interface in comparison with that of the Au/MoS_2 counterpart, we show in Fig. 8c, d how the In-*5p*$_z$ (pink filled line) and Au-*6s* (orange filled line) projected density of states (PDOS) evolve into the metal-contacting ① S-*3p* layer, ② Mo-*4d* layer, and ③ the outer S-*3p* layer PDOS of MoS_2 for the In/MoS_2 and Au/MoS_2 contacts, respectively. It is immediately notable that, while the Au-*6s* PDOS are uniformly distributed across the MoS_2 bandgap (Fig. 8d first panel), the In-*5p*$_z$ PDOS show energetically very asymmetric distribution such that they start from a negligible level near the MoS_2 VBM region and increase significantly toward the MoS_2 CBM region (Fig. 8c first panel). The MoS_2 VBM and CBM PDOS are mostly composed of Mo-*4d* orbitals (compare the second/fourth panels with the second panels in Fig. 8c, d). Then, we find for the In/MoS_2 contact case that very strong density of in-gap states are formed between E_F and MoS_2 CBM position (Fig. 8c third panel). As schematically depicted by the thick arrow in Fig. 8c, electrons injecting from In into these MoS_2 in-gap states then should result in the experimentally observed field-emission-type charge transport accompanied by a negligible effective ϕ_{SB}. On the other hand, the corresponding Mo-*4d* PDOS around E_F for the Au contact case are relatively marginal, making such a charge injection mechanism ineffective (schematically represented by a thin arrow in Fig. 8d). In Fig. 8e, f, we additionally visualized in real space the E_F-region In-MoS_2 and Au-MoS_2 hybridized DOS, respectively. The stronger hybridization between In and MoS_2 states than that between Au and MoS_2 states then provides an intuitive explanation how the Ohmic-like charge transport is achieved for the In/MoS_2 interface in spite of the very small interfacial charge transfer (see Fig. 3).

In summary, carrying out a combined experimental and theoretical investigation for an ultraclean vdW contact between an elemental metal In (without alloying) and semiconductor MoS_2, we revealed the mechanism of Ohmic charge transport across the In/MoS_2 vdW interface. For the single- and few-layer MoS_2 devices, the contact resistance decreased with decreasing temperatures for 100 ≤ T ≤ 300 K, indicating the field-emission mechanism for the Ohmic-like contact transport. The contact resistance was sensitive to the change of sheet resistance of MoS_2, rather than

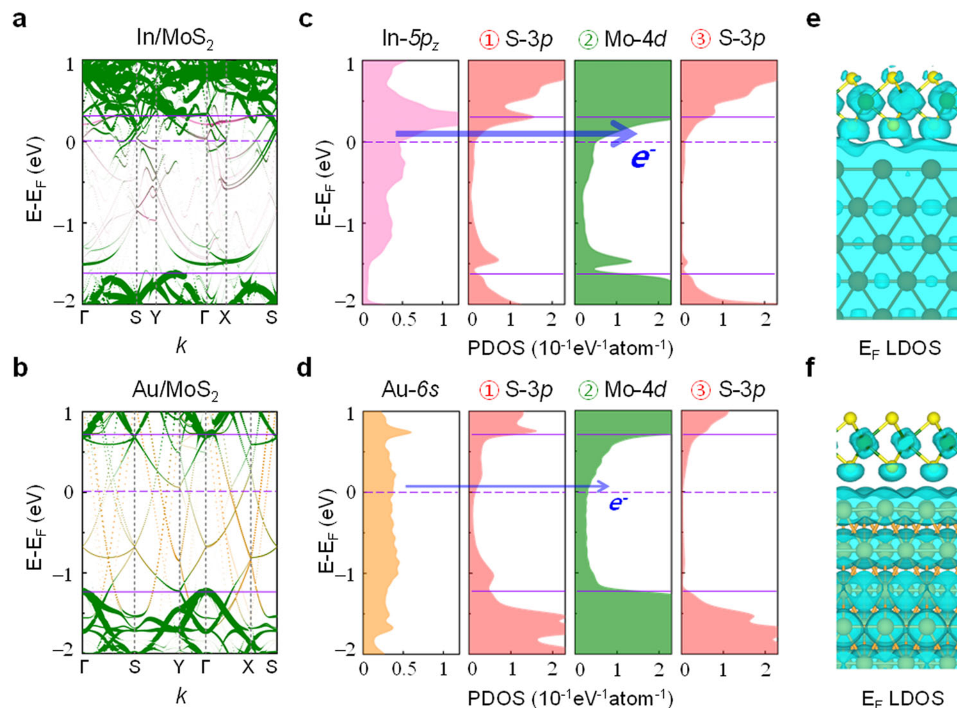

Fig. 8 Atomistic origins of the field emission-dominated charge transport across In/MoS_2 contacts. Projected band structures of the Mo-*4d* states (green-filled circle) for the **a** In/MoS_2 and **b** Au/MoS_2 interfaces. Shown together in **c** and **d** are the In-5p_z (pink filled circles) and Au-*6s* states (orange filled circles) contributions, respectively. The circle size is proportional to the weight of the projection of the wavefunctions. The PDOS of the In-5p_z (top left panel) and Au-*6s* (bottom left panel), ① metal-contacting S-*3p* (second panels), ② Mo-*4d* (third panels), and ③ outer S-*3p* (fourth panels) orbitals. In the second, third, and fourth panels, the upper and lower solid lines indicate the MoS_2 CBM and VBM levels, respectively. The arrows schematically show that the charge transport across the In/MoS_2 contact is much more efficient than that across the Au/MoS_2 counterpart, and the Ohmic-like charge transport is mediated by the large in-gap states formed around E_F of the In/MoS_2 interface. The local DOS in the range between E_F and E_F+0.2 eV overlaid over the **e** In/MoS_2 and **f** Au/MoS_2 interface models. The iso-surface level is 2.5×10^{-4} states eV^{-1} Å^{-3}.

that of the specific contact resistivity within the field-emission region. For the monolayer MoS_2 case, we achieved the contact resistance of ~1 kΩ μm at $T = 100$ K, which is the lowest value achieved by metal evaporations on MoS_2 to date. Our experimental findings were corroborated by DFT calculations, which showed that the In/MoS_2 contact has a weakened FLP due to the marginal interfacial charge transfer. Importantly, in spite of the weak interface dipole formation, we found that strong density of in-gap states are formed around MoS_2 CBM states and enable an Ohmic-like charge transport across the In/MoS_2 interface. Related with this identified mechanism, we comment that one of us previously predicted for semiconducting carbon nanotubes that a highly efficient charge injection across vdW metal contacts could be achieved via large in-gap states generated from topological defects within the sp^2 carbon network[28]. We thus suggest that seeking a mechanism of introducing strong density of in-gap states while maintaining the ideal contact geometry with weak charge transfer could prove to be a general strategy to simultaneously avoid FLP and minimize contact resistance for low-dimensional vdW materials[42].

METHODS

Device fabrication

We fabricated MoS_2 FETs on *h*-BN flakes, where the *h*-BN flakes were deposited onto a 300-nm-thick SiO_2/Si substrate by mechanical exfoliation. We then transferred a few-layer MoS_2 flake (HQ-graphene, Inc.) onto a selected *h*-BN flake[12,20]. For the electrical measurements, we deposited 100-nm-thick In electrodes across the MoS_2 channel, where the substrate holder was kept at ~100 K by flowing liquid nitrogen through it. The substrate cooling process leads to an important result; a uniform surface morphology of In film is achieved, which contrasts strongly with the usage of a room-temperature holder that produces a segregated granular film for at least up to ~70 nm thickness, as reported in our previous work (also see Supplementary Fig. 1)[21].

Raman spectroscopy

The Raman measurements were performed in a backscattering geometry at room temperature. An incident laser light with a wavelength of 514.5 nm was focused on the sample surface through an optical microscope objective lens (100×/0.9 NA). An excitation laser power was maintained less than 0.4 mW to avoid any laser-induced heating effects. Scattered light from the sample was dispersed through a monochromator with a 1200 grooves mm^{-1} grating and was collected using a thermoelectrically cooled charge-coupled device detector. For mapping measurements, Raman spectra were taken at the step of 0.5 μm over the area of 15 × 15 μm^2.

DFT calculations

We performed DFT calculations within the local density approximation (LDA)[43] using the SIESTA software[44]. The atomic cores were replaced by norm-conserving nonlocal pseudopotentials of the Troullier-Martins type[45], and double ζ-plus-polarization-level numerical atomic orbital basis sets were employed. Geometry optimizations were performed until the Hellmann-Feynman ionic forces were below 0.02 eV Å^{-1}. To check the reliability of geometries and electronic structures obtained within LDA in terms of vdW interactions, we also carried out DFT calculations using the DFT-D3 (ref. [46]) exchange-correlation functional. As in our earlier work[47], we obtained consistent results from LDA and DFT-D3 calculations (see Supplementary Figs. 3, 4 and Table 1).

DATA AVAILABILITY

The datasets generated during and/or analyzed during the current study are available from the corresponding author on reasonable request. All data generated or

analyzed during this study are included in this published article (and its Supplementary Information).

Received: 12 September 2020; Accepted: 25 November 2020;
Published online: 08 January 2021

REFERENCES

1. Manzeli, S., Ovchinnikov, D., Pasquier, D., Yazyev, O. V. & Kis, A. 2D transition metal dichalcogenides. *Nat. Rev. Mater.* **2**, 17033 (2017).
2. Li, C., Zhou, P. & Zhang, D. W. Devices and applications of van der Waals heterostructures. *J. Semicond.* **38**, 031005 (2017).
3. Xia, F., Wang, H., Xiao, D., Dubey, M. & Ramasubramaniam, A. Two-dimensional material nanophotonics. *Nat. Photonics* **8**, 899 (2014).
4. Allain, A., Kang, J., Banerjee, K. & Kis, A. Electrical contacts to two-dimensional semiconductors. *Nat. Mater.* **14**, 1195 (2015).
5. Schulman, D. S., Arnold, A. J. & Das, S. Contact engineering for 2D materials and devices. *Chem. Soc. Rev.* **47**, 3037 (2018).
6. Das, S., Chen, H. Y., Penumatcha, A. V. & Appenzeller, J. High performance multilayer MoS_2 transistors with scandium contacts. *Nano Lett.* **13**, 100 (2013).
7. Kim, C. et al. Fermi level pinning at electrical metal contacts of monolayer molybdenum dichalcogenides. *ACS Nano* **11**, 1588 (2017).
8. Yang, L. et al. Chloride molecular doping technique on 2D materials: WS_2 and MoS_2. *Nano Lett.* **14**, 6275–6280 (2014).
9. Wang, J. et al. High mobility MoS_2 transistor with low Schottky barrier contact by using atomic thick h-BN as a tunneling layer. *Adv. Mater.* **28**, 8302 (2016).
10. Cui, X. et al. Low-temperature Ohmic contact to monolayer MoS_2 by van der Waals bonded Co/h-BN electrodes. *Nano Lett.* **17**, 4781 (2017).
11. Leong, W. S. et al. Low resistance metal contacts to MoS_2 devices with nickel-etched-graphene electrodes. *ACS Nano* **9**, 869 (2015).
12. Cui, X. et al. Multi-terminal transport measurements of MoS_2 using a van der Waals heterostructure device platform. *Nat. Nanotechnol.* **10**, 534 (2015).
13. Kappera, R. et al. Phase-engineered low-resistance contacts for ultrathin MoS_2 transistors. *Nat. Mater.* **13**, 1128 (2014).
14. Liu, Y. et al. Approaching the Schottky-Mott limit in van der Waals metal-semiconductor junctions. *Nature* **557**, 696 (2018).
15. Wang, J. et al. Low-power complementary inverter with negative capacitance 2D semiconductor transistors. *Adv. Funct. Mat*er. **30**, 2003859 (2020).
16. Kong, L. et al. Doping-free complementary WSe_2 circuit via van der Waals metal integration. *Nat. Commun.* **11**, 1866 (2020).
17. Wang, Y. et al. Van der Waals contacts between three-dimensional metals and two-dimensional semiconductors. *Nature* **568**, 70 (2019).
18. Kim, B.-K. et al. Genuine Ohmic van der Waals contact between indium and MoS_2. Preprint at https://arxiv.org/abs/1904.10295 (2019).
19. Lau, C. S. et al. Quantum transport in two-dimensional WS_2 with high-efficiency carrier injection through indium alloy contacts. *ACS Nano* **14**, 13700–13708 (2020).
20. Dean, C. R. et al. Boron nitride substrates for high-quality graphene electronics. *Nat. Nanotechnol.* **5**, 722 (2010).
21. Choi, D.-H. et al. Van-der-Waals-gap tunneling spectroscopy for single-wall carbon nanotubes. *Carbon* **113**, 237 (2017).
22. Chakraborty, B. et al. Symmetry-dependent phonon renormalization in monolayer MoS_2 transistor. *Phys. Rev. B* **85**, 161403 (2012).
23. Somvanshi, D. et al. Nature of carrier injection in metal/2D-semiconductor interface and its implications for the limits of contact resistance. *Phys. Rev. B* **96**, 205423 (2017).
24. Lloyd, D. et al. Band gap engineering with ultralarge biaxial strains in suspended monolayer MoS_2. *Nano Lett.* **16**, 5836 (2016).
25. Li, H. et al. Optoelectronic crystal of artificial atoms in strain-textured molybdenum disulphide. *Nat. Commun.* **6**, 7381 (2015).
26. Hui, Y. Y. et al. Exceptional tunability of band energy in a compressively strained trilayer MoS_2 sheet. *ACS Nano* **7**, 7126 (2013).
27. Kim, Y.-H. & Kim, H. S. Anomalous length scaling of carbon nanotube-metal contact resistance: an ab initio study. *Appl. Phys. Lett.* **100**, 213113 (2012).
28. Kim, H. S., Lee, G. I., Kim, H. S., Kang, J. K. & Kim, Y.-H. Intrinsically low-resistance carbon nanotube-metal contacts mediated by topological defects. *MRS Commun.* **2**, 91 (2012).
29. Popov, I., Seifert, G. & Tomanek, D. Designing electrical contacts to MoS_2 monolayers: a computational study. *Phys. Rev. Lett.* **108**, 156802 (2012).
30. Farmanbar, M. & Brocks, G. First-principles study of van der Waals interactions and lattice mismatch at MoS_2/metal interfaces. *Phys. Rev. B* **93**, 085304 (2016).
31. Tung, R. T. The physics and chemistry of the Schottky barrier height. *Appl. Phys. Rev.* **1**, 011304 (2014).
32. Fivaz, R. & Mooser, E. Mobility of charge carriers in semiconducting layer structures. *Phys. Rev.* **163**, 743 (1967).
33. Kaasbjerg, K., Thygesen, K. S. & Jacobsen, K. W. Phonon-limited mobility in n-type single-layer MoS_2 from first principles. *Phys. Rev. B* **85**, 115317 (2012).
34. Kim, S. et al. High-mobility and low-power thin-film transistors based on multilayer MoS_2 crystals. *Nat. Commun.* **3**, 1011 (2012).
35. English, C. D., Shine, G., Dorgan, V. E., Saraswat, K. C. & Pop, E. Improved contacts to MoS_2 transistors by ultra-high vacuum metal deposition. *Nano Lett.* **16**, 3824 (2016).
36. Xia, F., Perebeinos, V., Lin, Y. M., Wu, Y. & Avouris, P. The origins and limits of metal-graphene junction resistance. *Nat. Nanotechnol.* **6**, 179 (2011).
37. Gong, C., Colombo, L., Wallace, R. M. & Cho, K. The unusual mechanism of partial Fermi level pinning at metal-MoS_2 interfaces. *Nano Lett.* **14**, 1714 (2014).
38. Guo, Y., Liu, D. & Robertson, J. 3D behavior of Schottky barriers of 2D transition-metal dichalcogenides. *ACS Appl. Mater. Interfaces* **7**, 25709 (2015).
39. Liu, Y., Stradins, P. & Wei, S. H. Van der Waals metal-semiconductor junction: Weak Fermi level pinning enables effective tuning of Schottky barrier. *Sci. Adv.* **2**, e1600069 (2016).
40. Zhong, H. et al. Interfacial properties of monolayer and bilayer MoS_2 contacts with metals: beyond the energy band calculations. *Sci. Rep.* **6**, 21786 (2016).
41. Kang, J., Liu, W., Sarkar, D., Jena, D. & Banerjee, K. Computational study of metal contacts to monolayer transition-metal dichalcogenide semiconductors. *Phys. Rev. X* **4**, 031005 (2014).
42. Leonard, F. & Talin, A. A. Electrical contacts to one- and two-dimensional nanomaterials. *Nat. Nanotechnol.* **6**, 773 (2011).
43. Ceperley, D. M. & Alder, B. J. Ground state of the electron gas by a stochastic method. *Phys. Rev. Lett.* **45**, 566 (1980).
44. Soler, J. M. et al. The SIESTA method for ab initio order-N materials simulation. *J. Phys. Condens. Matter* **14**, 2745 (2002).
45. Troullier, N. & Martins, J. L. Efficient pseudopotentials for plane-wave calculations. *Phys. Rev. B* **43**, 1993 (1991).
46. Grimme, S., Antony, J., Ehrlich, S. & Krieg, H. A consistent and accurate ab initio parametrization of density functional dispersion correction (DFT-D) for the 94 elements H-Pu. *J. Chem. Phys.* **132**, 154104 (2010).
47. Lee, J. et al. Origin and control of polyacrylonitrile alignments on carbon nanotubes and graphene nanoribbons. *Adv. Funct. Mater.* **28**, 1706970 (2018).

ACKNOWLEDGEMENTS

We acknowledge Prof. E. Hwang and Dr. J.-S. Park for fruitful discussion. This work was supported by the Korea Research Institute of Standards and Science (KRISS-2020-GP2020-0001) and the National Research Foundation of Korea (NRF) (Grant Nos. 2018R1A2A1A05078440, SRC2016R1A5A1008184, 2020R1F1A1075216, 2019R1A2C1003366, 2017R1A2B3009872, 2016M3A7B4024133, 2013M3A6B1078881, and 2017R1A4A1015400). Growth of hexagonal boron nitride crystals was supported by the Elemental Strategy Initiative conducted by the MEXT, Japan, Grant Number JPMXP0112101001, JSPS KAKENHI Grant Number JP20H00354 and the CREST (JPMJCR15F3), JST. Computational resources were provided by the KISTI Supercomputing Center (KSC-2018-C2-0032).

AUTHOR CONTRIBUTIONS

M.-H.B., J.-J.K, and Y.-H.K. conceived the research project. K.W. and T.T. grew the bulk *h*-BN. D.-H.C. and B.-K.K. fabricated the devices. D.-H.C. performed the TEM analysis. B.-K.K. performed the electrical measurements and analyzed the data with M.-H.B. H.K. and H.R. performed the Raman spectroscopy. T.-H.K. and Y.-H.K. performed the DFT calculations. M.-H.B, B.-K.K, T.-H.K., Y.-H.K., and J.-J.K. wrote the manuscript. All authors discussed the results and commented on the manuscript. B.-K.K., T.-H.K., and D.-H.C. contributed equally to this work.

COMPETING INTERESTS

The authors declare no competing interests.

ADDITIONAL INFORMATION

Supplementary information is available for this paper at https://doi.org/10.1038/s41699-020-00191-z.

Correspondence and requests for materials should be addressed to J.-J.K., Y.-H.K. or M.-H.B.

Reprints and permission information is available at http://www.nature.com/reprints

Publisher's note Springer Nature remains neutral with regard to jurisdictional claims in published maps and institutional affiliations.

Open Access This article is licensed under a Creative Commons Attribution 4.0 International License, which permits use, sharing, adaptation, distribution and reproduction in any medium or format, as long as you give appropriate credit to the original author(s) and the source, provide a link to the Creative Commons license, and indicate if changes were made. The images or other third party material in this article are included in the article's Creative Commons license, unless indicated otherwise in a credit line to the material. If material is not included in the article's Creative Commons license and your intended use is not permitted by statutory regulation or exceeds the permitted use, you will need to obtain permission directly from the copyright holder. To view a copy of this license, visit http://creativecommons.org/licenses/by/4.0/.

© The Author(s) 2021